

# Interlayer exciton in multilayer-monolayer van der Waals heterostructures

Qinghai Tan<sup>1</sup>, Abdullah Rasmita<sup>1</sup>, Zumeng Huang<sup>1</sup>, Sheng Liu<sup>1</sup>, Qihua Xiong<sup>1</sup>, and Wei-bo Gao<sup>1,2</sup>

<sup>1</sup>*Division of Physics and Applied Physics, School of Physical and Mathematical Sciences, Nanyang Technological University, 637371, Singapore*

<sup>2</sup>*The Photonics Institute and Centre for Disruptive Photonic Technologies, Nanyang Technological University, 637371, Singapore*

Interlayer excitons are tightly bounded electron and hole pairs in heterostructures with electrons and holes residing in different layers. They have a long lifetime, making them a promising platform for exploiting many-body interactions. However, the current research is mostly focused on monolayer-monolayer heterostructures. Here, we observed the photoluminescence from multilayer WSe<sub>2</sub>/monolayer MoS<sub>2</sub> heterostructures. We found that the temperature dependence of the interlayer exciton photoluminescence intensity, lifetime, and peak energy depends on the number of the WSe<sub>2</sub> layers. By comparing the optical transition energies in monolayer-monolayer and multilayer-monolayer heterostructures, we can extract the valence band shift of multilayer WSe<sub>2</sub>, which is otherwise only possible with sophisticated methods such as angle-resolved photoemission spectroscopy (ARPES). These findings expand our understanding of the interlayer excitons and bandgap engineering with the layer degree of freedom.

Layered transition metal dichalcogenides (TMDs) exhibit many novel physical properties, such as the layer-dependent electronic band structure [1-3], valley polarization [4-6], and nonlinear optical response [7-9]. The flexibility of stacking two different layered TMDs together to form the van der Waals heterostructures (HS) opens up new degrees of freedom to further expand its fascinating properties [10]. One of the most interesting aspects of the HS is the existence of the interlayer excitons (IXs), where the electrons and holes are separated into different layers. Because of the spatially indirect nature and the suppressed electron-hole exchange interaction, the IXs have a long lifetime [11-13], a high valley polarization degree [14], and a long exciton diffusion length even at room temperature [15]. Moreover, the Moiré IXs formed in a HS with a small stacking angle provides another degree of freedom to tune the optical and electronic properties of HS [16-19]. However, up to now, most reports on the IXs concerns only bilayer HS system [12,20-22] and, based on our knowledge, a detailed study of the effect of layers number has not been done. The question arises whether the number of TMDs layers can be an independent degree of freedom to tune the properties of IXs in multilayer HS.

On the other hand, the evolution of valance band maximum (VBM) and conduction band minimum (CBM) of TMDs with the number of layers plays fundamental importance in determining the properties of TMDs and the HS. However, each of the existing theoretical results is different due to the different choices in the approximation method, the lattice constant, and the interlayer distance

[23-26]. Moreover, due to the atomic thickness and the small size of few-layer TMDs, only limited experimental methods can be directly used to determine the evolution of the band with layers [2,23]. Some of these methods, such as the angle-resolved photoemission spectroscopy (ARPES), while can be used to obtain the overall band structure, requires sophisticated experimental condition such as ultrahigh vacuum and very clean sample surface [2,23]. An alternative is to use the IXs in the HS. In the HS with type-II band alignment, the IXs consists of conduction band electrons and valence band holes residing in different layers [12,26]. This layer separation makes it an excellent system to investigate the band shifts by monitoring the energy shift of the IXs while keeping one layer the same and changing the other layers. This method is simpler than ARPES since it does not require an ultrahigh vacuum and can be applied to sample with lower surface quality.

In this work, we studied the photoluminescence (PL) of the IXs from multilayer (mL) WSe<sub>2</sub>/monolayer (1L) MoS<sub>2</sub> HS. We found that the temperature dependence of the IXs PL is sensitive to the relative energy level between K and  $\Gamma$  point of WSe<sub>2</sub>. Based on the fitting result of the data to the theoretical model, we obtain the value of the energy difference between K and  $\Gamma$  point of multilayer WSe<sub>2</sub>. More importantly, we show that these IXs can be used to extract the energy shift of the valence band at the K point and the evolution of the VBM of WSe<sub>2</sub> with the number of layers. Our study opens a new way to control IXs by layer engineering and provides an effective way to determine the band shift of TMDs.

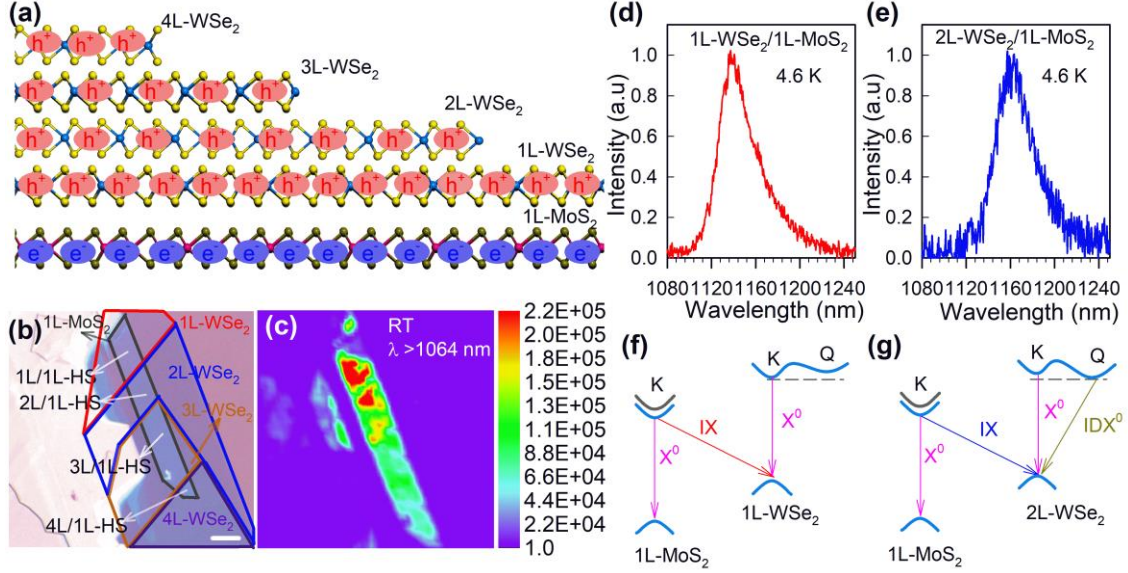


FIG. 1. (a) A schematic of the IXs in 1L MoS<sub>2</sub> and 1L-4L WSe<sub>2</sub> HS. The electrons and holes reside in MoS<sub>2</sub> and WSe<sub>2</sub> layers, respectively. (b) The optical microscope image of mL ( $m=1$  to 4) WSe<sub>2</sub>/1L MoS<sub>2</sub> HS (mL/1L HS) of the sample S1, the scale bar is 5  $\mu\text{m}$ . (c) PL intensity map of the IXs in HS shown in (b) at room temperature. A 1064 nm long pass (LP1064) is used. (d-e) The PL spectra of 1L/1L and 2L/1L HS at 4.6 K. (f-g) A schematic of the transition of the intralayer excitons ( $X^0$ ), the indirect intralayer excitons ( $IDX^0$ ), and the interlayer exciton (IX).

Figure 1(a) shows a schematic of multilayer HS formed by a monolayer (1L) MoS<sub>2</sub> and 1L to 4L WSe<sub>2</sub>. The electrons and holes are separated into the MoS<sub>2</sub> layer and the WSe<sub>2</sub> layers, respectively, forming the IXs. Fig. 1(b) shows a typical optical image for mL (here  $m=1$  to 4) WSe<sub>2</sub>/1L MoS<sub>2</sub> HS (mL/1L HS). The monolayer MoS<sub>2</sub> and the few-layer WSe<sub>2</sub> are first exfoliated mechanically from bulk crystals on polydimethylsiloxane (PDMS) stamps, and then transferred to form the HS by a dry transfer method. The sample preparation, optical setup detail, and the characterization of the number of layers using the Raman spectroscopy can be found in the supplementary information [27].

Figure 1(c) shows the PL intensity map ( $\lambda > 1064\text{ nm}$ ) in these HS at room temperature. The bright area matches well with the HS area, suggesting that the IXs are formed in these HS samples. As a comparison, we measured the intralayer exciton PL spectra in the visible range in the area of 1L MoS<sub>2</sub>, 1L WSe<sub>2</sub>, 2L WSe<sub>2</sub>, and HS at room temperature, as well as the IXs in 1L/1L HS (see Fig. S2(a-c) in Ref. [27]). The PL intensity of the intralayer exciton in the HS region shows a significant attenuation, implying that an efficient charge transfer across layers leads to the quenching of the intralayer exciton emission [28]. More HS sample images and similar Raman and PL spectra characterizations are presented in Fig. S3 and S4 in the supplementary information [27].

Figure 1(d) and 1(e) show the PL spectra of IX of 1L/1L and 2L/1L HS region at low temperature, respectively. We should note that the near-infrared region emission wavelength of IX in 1L/1L HS is far away from the emission of intralayer exciton [28], which can help us to avoid the influences of intralayer excitons by using a 1064 nm long pass.

Figure 1(f) and 1(g) show the schematic of IX transitions in 1L/1L and 2L/1L HS. In both cases, due to the type II band alignment and the large band offset between MoS<sub>2</sub> and WSe<sub>2</sub> [29,30], the IXs consist of electrons located in CBM of MoS<sub>2</sub> and holes located in VBM of WSe<sub>2</sub>. Since both MoS<sub>2</sub> CBM and WSe<sub>2</sub> VBM are located at K valley, the lowest energy IX is a momentum direct (K-K) exciton. Moreover, considering the spin-orbit coupling induced conduction band splitting of MoS<sub>2</sub> [31,32], the bright IX has lower energy than the dark one. This statement is true for both 1L/1L HS and 2L/1L HS. In contrast, while the lowest energy intralayer exciton in 1L WSe<sub>2</sub> is a momentum-direct exciton, it is a momentum-indirect exciton in bilayer WSe<sub>2</sub>. This is because, for bilayer WSe<sub>2</sub>, the CBM is located at Q valley while VBM is at K point [2]. Hence, in contrast to the bilayer WSe<sub>2</sub>, the bilayer WSe<sub>2</sub>/1L MoS<sub>2</sub> HS has a direct bandgap. More data on the intralayer exciton in 1L/1L and 2L/1L HS is presented in Ref. [27].

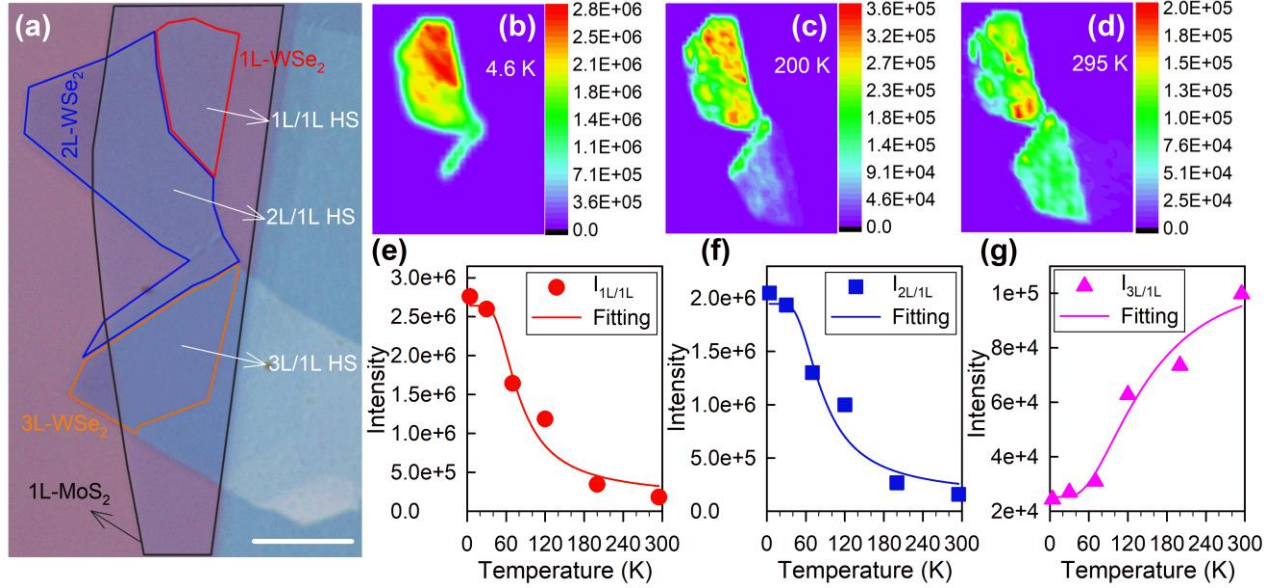


FIG. 2. (a) The optical microscope image of  $mL\text{-WSe}_2/1L\text{-MoS}_2$  ( $m=1$  to 3) HS of the sample S2. The scale bar is  $10\ \mu\text{m}$ . (b-d) The PL intensity map of the IXs at 4.6 K, 200 K, and 295 K, respectively. (e-f) The PL intensity of IXs of  $mL/1L$  HS as a function of temperature. The solid lines are the fitting results.

Temperature-dependent PL measurement is used to confirm the transition nature of IXs in  $mL/1L$  HS further. The HS sample image and PL mapping at different temperatures are shown in Fig. 2 (a-d). The PL intensity of the IXs in  $1L/1L$  HS decreases as the temperature is increased (Fig. 2(e)), which is consistent with the case of monolayer  $\text{MoS}_2$  intralayer exciton [31,33]. This observation can be understood by considering that the bright IX is the lowest exciton energy level in  $1L/1L$  HS. As the temperature is increased, the bright IXs population will decrease since there is a higher probability that phonon can scatter the bright IXs to dark states with higher energy levels. Interestingly, the temperature dependence for IXs in  $2L/1L$  HS shows similar behavior to the  $1L/1L$  case, as shown in Fig. 2(f). This further confirms that the IXs in  $2L/1L$  HS is from the K-K transition.

In contrast to the  $1L/1L$  and  $2L/1L$  case, when the number of  $\text{WSe}_2$  layers is more than two in  $mL/1L$  HS (e.g.,  $m=3$ ), the PL intensity of the IXs tends to increase with increasing temperature (Fig. 2(g)). Since electrons are located in K valley of  $\text{MoS}_2$  in all cases, this indicates that the VBM from multilayer  $\text{WSe}_2$  changes from K to  $\Gamma$  point when the number of layers is increased to three. We note that these results are consistent with the recent direct measurement of the valance band of  $1L\text{-}3L\ \text{WSe}_2$  by the micrometer-scale angle-resolved photoemission spectroscopy (microARPES) [2].

Figure 3(a) illustrates the IXs transitions and the energy levels in  $1L/1L$  HS and  $3L/1L$  HS. The fact that the  $\text{WSe}_2$  VBM is in  $\Gamma$  means that the hole prefers to be in  $\Gamma$  instead

of K point. This implies that the indirect IXs have lower energy than the direct ones. As a consequence, the exciton population at low temperatures is dominated by indirect IXs. The radiative emission of the indirect IXs is largely suppressed due to the mismatch between electron and hole momentum. As the temperature increases, more phonons lead to an increase in the scattering of the hole from  $\Gamma$  to K point, which results in the increased IXs PL intensity. Considering both the bright-dark and K- $\Gamma$  transition, the rate equation model for both  $(m=1,2)L/1L$  and  $(m>2)L/1L$  can be derived (see Fig. 3). As shown in Fig. 2(e-g) the model can fit the data well. Based on the fitting result, we obtain the dark-bright energy separation,  $\Delta E_c = 20 \pm 8$

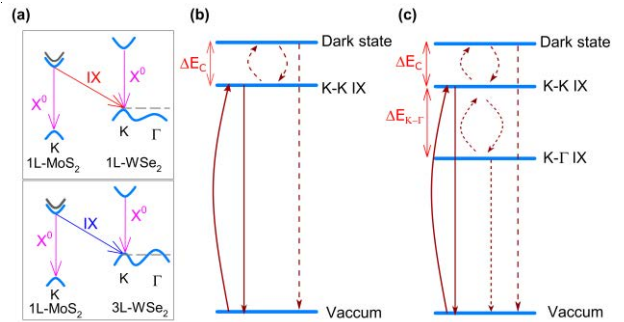


FIG. 3 (a) Illustration of the IX in  $1L\text{-MoS}_2/1L\text{-WSe}_2$  and  $3L\text{-WSe}_2/1L\text{-MoS}_2$  HS. (b,c) Rate equation model for  $(m=1,2)L/1L$  HS and  $(m>2)L/1L$  HS, respectively. The dashed brown lines show non-radiative dark transition. The solid brown lines are the optically active transition. The total population is conserved.

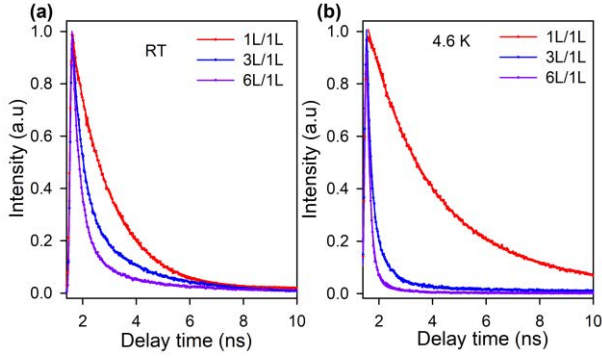


FIG. 4 (a-b) Time-resolved PL of mWSe<sub>2</sub>/1L HS (sample S3) at room temperature and low temperature, respectively.

meV, and the energy difference between WSe<sub>2</sub> K and  $\Gamma$  point,  $\Delta E_{K-\Gamma} = 19 \pm 4$  meV. These values are consistent with previously reported results [2,32]. More experimental results (Fig. S7) and detail about the model are presented in Ref. [27].

Additionally, we also measured the layer dependence of the IXs PL lifetime both at low (4.6 K) and room temperature (Fig. 4). The lifetime in 1L/1L HS is in the ns regime, which is consistent with previously reported IXs results [12,22]. Three main results can be observed here, (1) the lifetime decreases as the number of WSe<sub>2</sub> layers is increased. (2) In mWSe<sub>2</sub>/1L HS ( $m > 2$ ), the lifetime is longer at room temperature as compared to 4.6K. (3) In 1L/1L case, the lifetime is shorter at room temperature as compared to 4.6K. This observation is consistent with our model. First, for mWSe<sub>2</sub>/1L HS ( $m > 2$ ), K- $\Gamma$  IX has a lower energy level than K-K IX. It provides additional efficient decay channel. With layer number increasing, this decay channel becomes more efficient and thus the lifetime is decreased. Second, for mWSe<sub>2</sub>/1L HS ( $m > 2$ ), as the temperature is increased, due to a higher number of phonons, the decay channel from K-K IX to K- $\Gamma$  IX is getting less efficient. This results in a longer lifetime as the temperature is increased. Third, for 1L/1L case, K- $\Gamma$  IX is far above K-K IX energy level and will not affect the IX lifetime. Instead, it is affected by the dark state above K-K IX energy level. Therefore, it shows a reversed temperature dependence as compared to mWSe<sub>2</sub>/1L HS case ( $m > 2$ ).

Our results also show that IX peak energy depends on the number of WSe<sub>2</sub> layers. As illustrated in Fig. 5a, on a single HS sample with monolayer MoS<sub>2</sub> combined with either monolayer WSe<sub>2</sub> or multilayer WSe<sub>2</sub>, the electron locates at the same energy, i.e., the CBM of MoS<sub>2</sub>. Hence, in contrast with the WSe<sub>2</sub> intralayer exciton which is affected by both VBM and CBM of WSe<sub>2</sub>, the IX energy in mWSe<sub>2</sub>/1L HS is only affected by the change in VBM of WSe<sub>2</sub>. Therefore, we can monitor the WSe<sub>2</sub> VBM shifts by measuring the

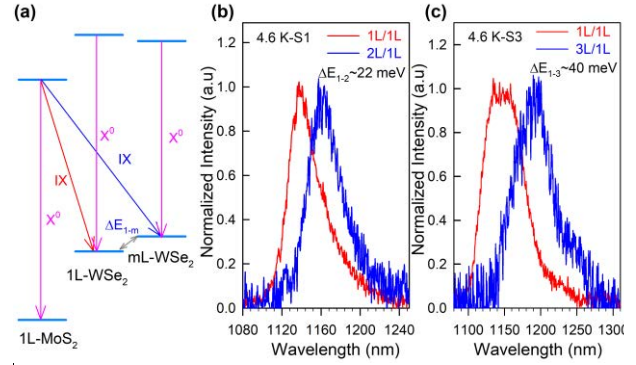


FIG. 5 (a) Illustration of the scheme to determine the VBM shift of mWSe<sub>2</sub> by monitoring the IXs emission energy peak. (b,c) Comparison between the PL spectra of 1L/1L HS vs. 2L/1L HS, and 1L/1L HS vs. 3L/1L HS, respectively, showing the energy difference of the IXs emission in these HS. S1 and S3 represent two different samples.

optical energy shifts from IXs in 1L/1L HS and mWSe<sub>2</sub>/1L HS. As shown in Fig. 5b, the valence band K point energy shift from monolayer WSe<sub>2</sub> to bilayer WSe<sub>2</sub> is determined to be  $\sim 22$  meV. A similar shift  $\sim 19$  meV is observed in sample S2, as shown in Fig. S9 in Ref. [27]. In contrast, the VBM shift in trilayer WSe<sub>2</sub> with respect to monolayer WSe<sub>2</sub> is  $\sim 40$  meV (Fig. 5c). These values are consistent with previously reported results obtained using microARPES [2]. We should note that the optical transition can have a slight energy difference for different samples due to the difference in stacking angles [16] and sample quality. Therefore, the monolayer-monolayer HS and monolayer-multilayer HS have to be from the same sample in the method above and they have to be measured in the same situation to get the best estimation for the layer dependence of the valence band shift.

In conclusion, we observed the IXs in multilayer WSe<sub>2</sub>/monolayer MoS<sub>2</sub> heterostructures. We found that, as the number of the WSe<sub>2</sub> layers is increased, the temperature dependence of the IXs PL changes dramatically, indicating the WSe<sub>2</sub> VBM location transition from K to  $\Gamma$  point. Furthermore, we show that the band shift of the WSe<sub>2</sub> VBM at K point in the few-layer WSe<sub>2</sub> can be determined from the change in the IXs PL spectra in multilayer HS. Our study opens an opportunity for layer engineering of the IXs and provides a convenient method to determine the energy shift of CBM and VBM in multilayer TMD materials.

## Acknowledgments

We acknowledge the financial support from the Singapore National Research Foundation through a Singapore 2015

NRF fellowship grant (NRF-NRFF2015-03), Singapore Ministry of Education (MOE2016-T2-2-077 and MOE2011-T3-1-005), A\*Star QTE programme.

\*Correspondence to [wbgao@ntu.edu.sg](mailto:wbgao@ntu.edu.sg)

- 
- [1] A. Splendiani, L. Sun, Y. Zhang, T. Li, J. Kim, C.-Y. Chim, G. Galli, and F. Wang, *Nano Lett.* **10**, 1271 (2010).
- [2] P. V. Nguyen *et al.*, *Nature* **572**, 220 (2019).
- [3] K. F. Mak, C. Lee, J. Hone, J. Shan, and T. F. Heinz, *Phys. Rev. Lett* **105**, 136805 (2010).
- [4] X. Xu, W. Yao, D. Xiao, and T. F. Heinz, *Nat. Phys.* **10**, 343 (2014).
- [5] H. Tornatzky, A.-M. Kaulitz, and J. Maultzsch, *Phys. Rev. Lett* **121**, 167401 (2018).
- [6] D. Xiao, G.-B. Liu, W. Feng, X. Xu, and W. Yao, *Phys. Rev. Lett* **108**, 196802 (2012).
- [7] A. Autere, H. Jussila, Y. Dai, Y. Wang, H. Lipsanen, and Z. Sun, *Adv. Mater.* **30**, 1705963 (2018).
- [8] D. S. Wild, E. Shahmoon, S. F. Yelin, and M. D. Lukin, *Phys. Rev. Lett* **121**, 123606 (2018).
- [9] X. Yin, Z. Ye, D. A. Chenet, Y. Ye, K. O'Brien, J. C. Hone, and X. Zhang, *Science* **344**, 488 (2014).
- [10] A. K. Geim and I. V. Grigorieva, *Nature* **499**, 419 (2013).
- [11] C. Jiang, W. Xu, A. Rasmitha, Z. Huang, K. Li, Q. Xiong, and W.-b. Gao, *Nat. Commun.* **9**, 753 (2018).
- [12] P. Rivera *et al.*, *Nat. Commun.* **6**, 6242 (2015).
- [13] J. Kim *et al.*, *Sci. Adv.* **3**, e1700518 (2017).
- [14] L. Zhang, R. Gogna, G. W. Burg, J. Horng, E. Paik, Y.-H. Chou, K. Kim, E. Tutuc, and H. Deng, *Phys. Rev. B* **100**, 041402 (2019).
- [15] D. Unuchek, A. Ciarrocchi, A. Avsar, K. Watanabe, T. Taniguchi, and A. Kis, *Nature* **560**, 340 (2018).
- [16] E. M. Alexeev *et al.*, *Nature* **567**, 81 (2019).
- [17] C. Jin *et al.*, *Nature* **567**, 76 (2019).
- [18] K. L. Seyler, P. Rivera, H. Yu, N. P. Wilson, E. L. Ray, D. G. Mandrus, J. Yan, W. Yao, and X. Xu, *Nature* **567**, 66 (2019).
- [19] K. Tran *et al.*, *Nature* **567**, 71 (2019).
- [20] P. Rivera, H. Yu, K. L. Seyler, N. P. Wilson, W. Yao, and X. Xu, *Nat. Nanotech.* **13**, 1004 (2018).
- [21] J. Kunstmann *et al.*, *Nat. Phys.* **14**, 801 (2018).
- [22] P. Rivera, K. L. Seyler, H. Yu, J. R. Schaibley, J. Yan, D. G. Mandrus, W. Yao, and X. Xu, *Science* **351**, 688 (2016).
- [23] F. Bussolotti, H. Kawai, Z. E. Ooi, V. Chellappan, D. Thian, A. L. C. Pang, and K. E. J. Goh, *Nano Futures* **2**, 032001 (2018).
- [24] A. Kuc, N. Zibouche, and T. Heine, *Phys. Rev. B* **83**, 245213 (2011).
- [25] M. H. Naik and M. Jain, *Phys. Rev. B* **95**, 165125 (2017).
- [26] C. Jin, E. Y. Ma, O. Karni, E. C. Regan, F. Wang, and T. F. Heinz, *Nat. Nanotech.* **13**, 994 (2018).
- [27] See Supplemental Material at [URL] for more experimental results and discussions.
- [28] Y. Liu *et al.*, *Sci. Adv.* **5**, eaav4506 (2019).
- [29] J. Kang, S. Tongay, J. Zhou, J. Li, and J. Wu, *Appl. Phys. Lett.* **102**, 012111 (2013).
- [30] M.-H. Chiu *et al.*, *Nat. Commun.* **6**, 7666 (2015).
- [31] X.-X. Zhang, Y. You, S. Y. F. Zhao, and T. F. Heinz, *Phys. Rev. Lett.* **115**, 257403 (2015).
- [32] J. P. Echeverry, B. Urbaszek, T. Amand, X. Marie, and I. C. Gerber, *Phys. Rev. B* **93**, 121107 (2016).
- [33] S. Tongay, J. Zhou, C. Ataca, K. Lo, T. S. Matthews, J. Li, J. C. Grossman, and J. Wu, *Nano Lett.* **12**, 5576 (2012).

# Supplementary Materials for

## “Interlayer exciton in multilayer-monolayer van der Waals heterostructures”

Qinghai Tan<sup>1</sup>, Abdullah Rasmita<sup>1</sup>, Zumeng Huang<sup>1</sup>, Sheng Liu<sup>1</sup>, Qihua Xiong<sup>1</sup>, and Wei-bo Gao\*<sup>1,2</sup>

<sup>1</sup>*Division of Physics and Applied Physics, School of Physical and Mathematical Sciences, Nanyang Technological University, 637371, Singapore*

<sup>2</sup>*The Photonics Institute and Centre for Disruptive Photonic Technologies, Nanyang Technological University, 637371, Singapore*

### Section I: Experimental methods

The monolayer MoS<sub>2</sub> and few-layer WSe<sub>2</sub> are first exfoliated mechanically from bulk crystals on polydimethylsiloxane (PDMS) stamps, and then transferred onto ultralow doping Si substrate that covered by 285nm SiO<sub>2</sub>, to form the heterostructures (HS) by a dry transfer method. Then the HS samples were annealed under ultrahigh vacuum (around 10<sup>-6</sup> mbar) at 200 °C for 3 hours. The photoluminescence (PL) intensity map was detected by using an infrared superconducting single-photon detector. The PL spectra were obtained by a spectrometer (Andor Shamrock) with a CCD detector. Unless otherwise stated, a laser with 726 nm was used as the excitation source. A 50x objective lens (NA=0.65) is used to collect the signal. The sample temperature is controlled using a cryostation (Montana Instruments). For all PL measurements of the interlayer exciton, a 1064 nm long-pass filter is used to cut the laser and intralayer exciton signals. The Raman spectra were measured at room temperature using the T64000 Raman system equipped with a liquid-nitrogen-cooled CCD. The excitation wavelength for Raman spectra measurement is 532 nm. In all of the optical measurements, the laser power is below 100 μW.

### Section II: Raman and PL measurements of WSe<sub>2</sub>, MoS<sub>2</sub> and mL-WSe<sub>2</sub>/1L-MoS<sub>2</sub> HS

To understand the role of interlayer coupling between HS interface, we measured the ultralow to high-frequency Raman spectra of 1L to 4L WSe<sub>2</sub> and the heterostructures (HS) region (Fig. S1(a)). In the high-frequency range (above 100 cm<sup>-1</sup>), in addition to the E<sub>2g</sub><sup>1</sup> and A<sub>1g</sub> modes from WSe<sub>2</sub> and MoS<sub>2</sub>, two more feature modes are observed in 1L-WSe<sub>2</sub>/1L-MoS<sub>2</sub> HS region. These two modes are the Raman-inactive E<sub>2g</sub><sup>2</sup> mode (~285 cm<sup>-1</sup>) in monolayer MoS<sub>2</sub> and the B<sub>2g</sub><sup>1</sup> (~310 cm<sup>-1</sup>) mode in monolayer WSe<sub>2</sub>. Both are activated in 1L/1L HS, owing to the reduced symmetry of the HS [1,2]. For the same reason, more feature modes are observed in mL/1L HS than in multilayer WSe<sub>2</sub>. In the ultralow frequency range (below 50 cm<sup>-1</sup>), we found a series of shear (S) and layer breathing (LB) modes. Their mode frequencies are layer dependent for layered 2D materials [3,4]. We note that the S modes in mL/1L HS are almost the same with mL WSe<sub>2</sub>, suggesting that these modes are originated from mL WSe<sub>2</sub>. On the other hand, the LB modes in mL/1L HS behaves like (1+m)L WSe<sub>2</sub>. For example, in the 1L/1L HS region, a new LB mode is observed with a frequency slightly larger than that in bilayer WSe<sub>2</sub>. A similar case has also been found in the twisted multilayer graphene [5].

The interlayer coupling strength can be represented by the coupling force constant per unit area,

$\alpha$ . The value of  $\alpha$  can be obtained directly from the frequency of the LB mode in the bilayer 2D  $\text{MX}_2$  (M=Mo, W; X=S, Se) materials by the formula [3]  $\alpha = 2\mu[\pi c\omega_{LB}(2)]^2$ , where  $c$  is speed of light,  $\alpha$  is the force constant per unit area between the adjacent layers, and  $\mu = m_M + 2m_X$  with  $m_M$  and  $m_X$  are the mass of the M and X component, respectively [1,3]. The frequencies of the LB modes are around  $41 \text{ cm}^{-1}$ ,  $27.6 \text{ cm}^{-1}$ , and  $31 \text{ cm}^{-1}$  in bilayer  $\text{MoS}_2$ ,  $\text{WSe}_2$ , and HS, respectively. Therefore, the interlayer coupling strength in multilayer  $\text{WSe}_2$  is around 96.8% of multilayer  $\text{MoS}_2$ , while in the HS, it is approximately 94.5% of multilayer  $\text{WSe}_2$ .

Given the force constant, we can calculate the frequencies of the LB modes in multilayer  $\text{WSe}_2$  by using the linear chain model [3,4]. Fig. S1(b) shows the calculated frequencies of LB modes in 1L to 5L  $\text{WSe}_2$  as well as the experimental results of LB modes in 1L to 4L  $\text{WSe}_2$  and its HS region. As can be seen from this figure, the theoretical results agree well with the experimental results. Moreover, we also measured the PL map and Raman spectra of another three multilayer HS samples, including one 1L- $\text{WSe}_2$ /mL- $\text{MoS}_2$  (m=2,3) HS sample, as shown in Figure S3-S4, and got similar results.

Figure S2 (a-b) show the intralayer exciton of 1L- $\text{MoS}_2$ , 1L- $\text{WSe}_2$ , 2L- $\text{WSe}_2$ , 1L/1L HS, and 2L/1L HS at room temperature with 532 nm excitation. Because of the effect of the  $\text{MoS}_2$  layer (the interlayer coupling and charge transfer between  $\text{MoS}_2$  and  $\text{WSe}_2$  layers), besides the PL intensity attenuation, the  $X^0$  peak of  $\text{WSe}_2$  in 1L/1L HS and 2L/1L HS shows a redshift from around 748 nm to 756 nm and 762 nm to 770 nm, respectively. The  $X^0$  peak of  $\text{MoS}_2$  in 1L/1L HS and 2L/1L HS has a similar small redshift from around 656 nm to 661 nm. Furthermore, we didn't observe any new peaks in the range of 600 nm to 950 nm, except the direct and indirect intralayer exciton ( $X_0$ ,  $\text{IDX}_0$ ). Fig. S2(c) shows the PL spectrum of interlayer exciton in the 1L/1L HS region at room temperature. The emission wavelength is around 1220 nm, far away from the emission range of the intralayer exciton of  $\text{WSe}_2$  and  $\text{MoS}_2$ .

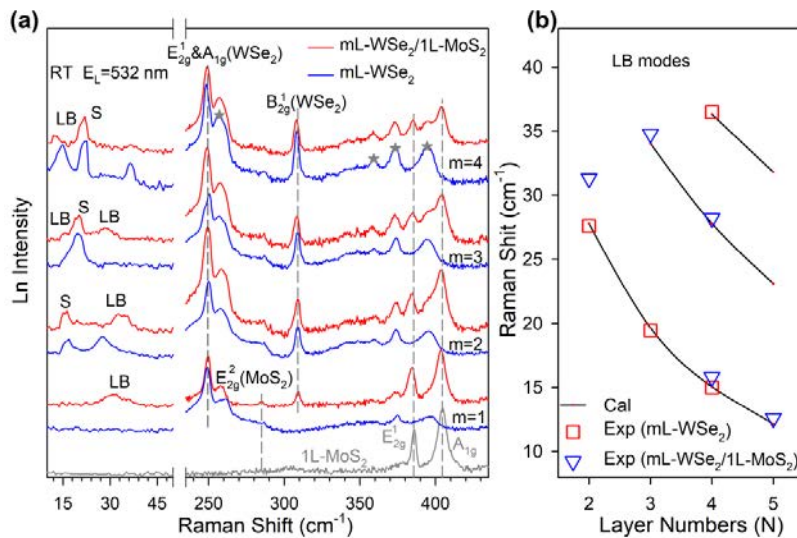


FIG. S1. (a) The Raman spectra of mL  $\text{WSe}_2$  and mL- $\text{WSe}_2$ /1L- $\text{MoS}_2$  (m=1 to 4) heterostructures (HS) (S1). (b) The calculated layer breathing (LB) modes and the experimental results of mL  $\text{WSe}_2$  and mL/1L (m=1 to 4) HS.

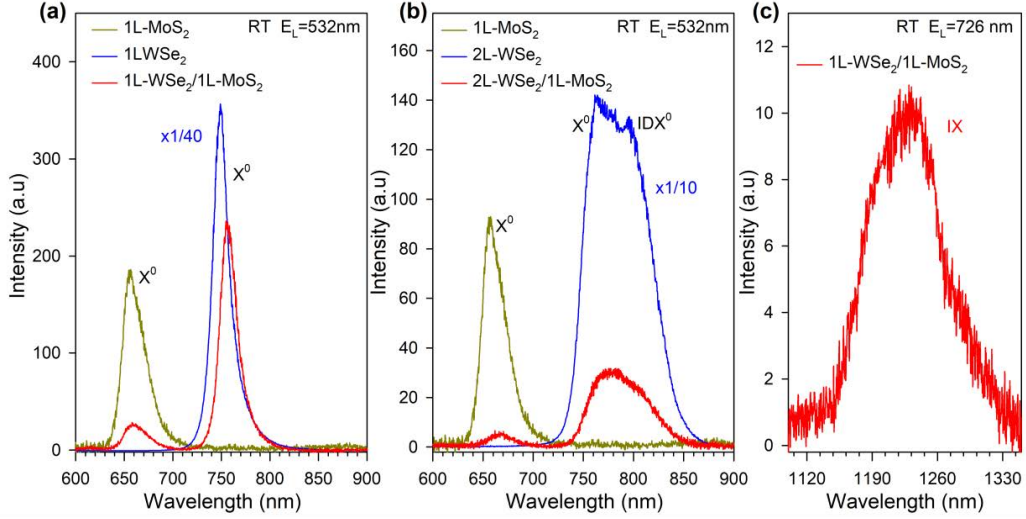


FIG. S2. (a-b) The PL spectra of 1L-MoS<sub>2</sub>, 1L-WSe<sub>2</sub>, 2L-WSe<sub>2</sub>, 1L/1L, and 2L/1L HS region at room temperature (RT) with 532 nm excitation.  $X^0$  represents direct intralayer exciton, and  $IDX^0$  represents indirect intralayer exciton. (c) The PL spectrum of IXs at 1L/1L HS region at room temperature with 726 nm excitation.

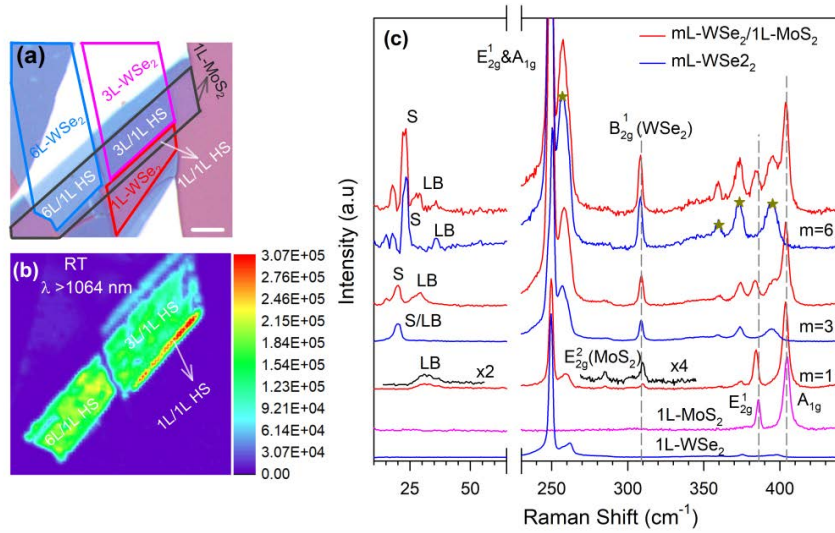


FIG. S3. (a) The optical microscope image of mL/1L ( $m=1, 3, 6$ ) HS (sample S3). (b) The PL intensity map of IXs in HS of sample S3 at room temperature. A 1064 nm long pass (LP1064) and 726 nm excitation are used. (c) The Raman spectra of mL WSe<sub>2</sub> and mL/1L HS.



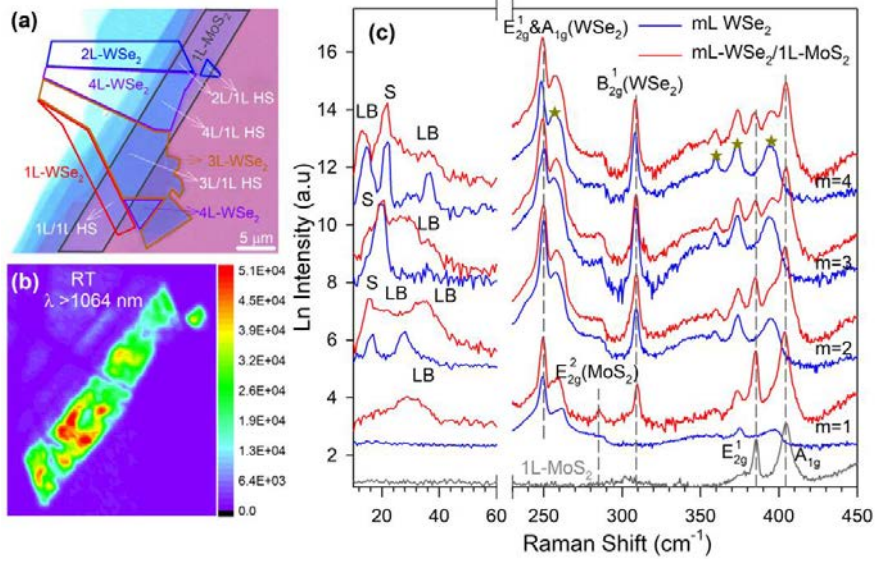


FIG. S4. The optical microscope image of mL/1L ( $m=1$  to 4) HS (sample S4). (b) The PL intensity map of IXs in HS of sample S4 at room temperature. A 1064 nm long pass (LP1064) and 726 nm excitation are used. (c) The Raman spectra of mL WSe<sub>2</sub> and mL/1L HS.

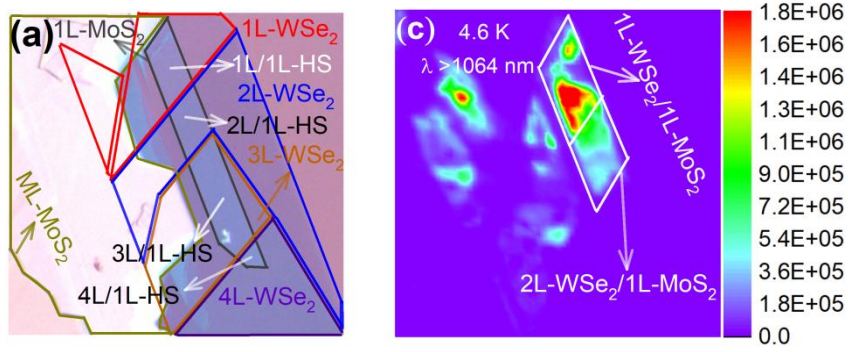


FIG. S5. (b) The optical microscope image mL/1L HS (sample S1) similar to Fig. 1b in the main text. (c) The PL intensity map of the interlayer exciton in sample S1 at 4.6 K. A 1064 nm long pass (LP1064) and 726 nm excitation are used.

### Section III: Temperature-dependent PL mapping measurement of IXs in mL-WSe<sub>2</sub>/1L-MoS<sub>2</sub>

Here, we give a simple rate equation model to explain the temperature dependence of the IXs emission in mL/1L HS. We consider two different cases:

- \*) Case 1: the WSe<sub>2</sub> valence band maximum (VBM) is in K point
- \*) Case 2: the WSe<sub>2</sub> VBM is in  $\Gamma$  point

#### Case 1

As described in the main text, Case 1 is relevant for 1L/1L HS and 2L/1L HS. In this case, the K (MoS<sub>2</sub>)-K (WSe<sub>2</sub>) bright IX is the IX state with the lowest energy. Due to coupling with phonon, it can be scattered to a higher dark state (i.e., its emission is non-radiative or cannot be collected). Hence, the intensity decrease as the temperature is increased.

The rate equation of the model is shown in Fig. S6(a). The IXs emission intensity can be expressed as

$$I(T) = \frac{I_L}{1 + A \exp\left(-\frac{\Delta E_C}{k_B T}\right)} \quad (S1)$$

where  $T$  is the sample temperature,  $k_B$  is Boltzmann constant,  $I_L$  is the intensity of the IXs emission at low temperature,  $\Delta E_C$  is the energy difference between dark state and bright K-K IX state, and  $A$  are the fitting parameters described in Fig. S6. We used  $\{I_L, A, \Delta E_C\}$  as the fitting parameters. The fitting results for sample S2 and S3 are shown in Fig. 2(e,f) in the main text and Fig. S7(e), respectively. As can be seen from these figures, the model fits the data quite well.

### Case 2

As described in the main text, Case 2 is relevant for mL ( $m > 2$ )/1L HS. In this case, the K (MoS<sub>2</sub>)-K (WSe<sub>2</sub>) bright IX is not the IX state with the lowest energy. Instead, the momentum indirect K- $\Gamma$  IX state is the IX state with the lowest energy level. Due to its indirect nature, the K- $\Gamma$  IXs radiative emission is largely suppressed at low temperatures.

At low temperatures, most of the IX population is in K- $\Gamma$  IXs state, which results in weak IXs emission. Due to coupling with phonon, K- $\Gamma$  IXs state can be scattered to the bright K-K IXs state at a higher temperature. This increases the IXs emission intensity as the temperature is increased.

The rate equation of the model is shown in Fig. S6(b). The IXs emission intensity can be expressed as

$$I(T) = \frac{I_L \left( P + Q \exp\left(-\frac{\Delta E_{K-\Gamma}}{k_B T}\right) \right)}{1 + \left( 1 + A \exp\left(-\frac{\Delta E_C}{k_B T}\right) \right) \left( P + Q \exp\left(-\frac{\Delta E_{K-\Gamma}}{k_B T}\right) \right)} \quad (S2)$$

where  $\{I_L, T, k_B, A, \Delta E_C\}$  is the same as in 1L/1L case (see equation (S1)),  $\Delta E_{K-\Gamma}$  is the energy difference between K-K and K- $\Gamma$  IXs state, and  $\{P, Q\}$  are fitting parameters described in Fig. S6.

We used  $\{P, Q, \Delta E_{K-\Gamma}\}$  as the fitting parameters while  $\{I_L, A, \Delta E_C\}$  is obtained from the fitting result of IXs emission in 1L/1L HS. The fitting results for sample S2 and S3 are shown in Fig. 2(g) in the main text and Fig. S7(f), respectively. We found the fitted value for  $\Delta E_{K-\Gamma}$  is consistent with recent experimental results [6]. Fig. S7(f) shows that, as the temperature is increased, the IXs emission in 6L/1L HS increases faster than the IXs emission in 3L/1L. This can be attributed to the larger energy difference between K and  $\Gamma$  valence band ( $\Delta E_{K-\Gamma}$ ) in 6L/1L HS.

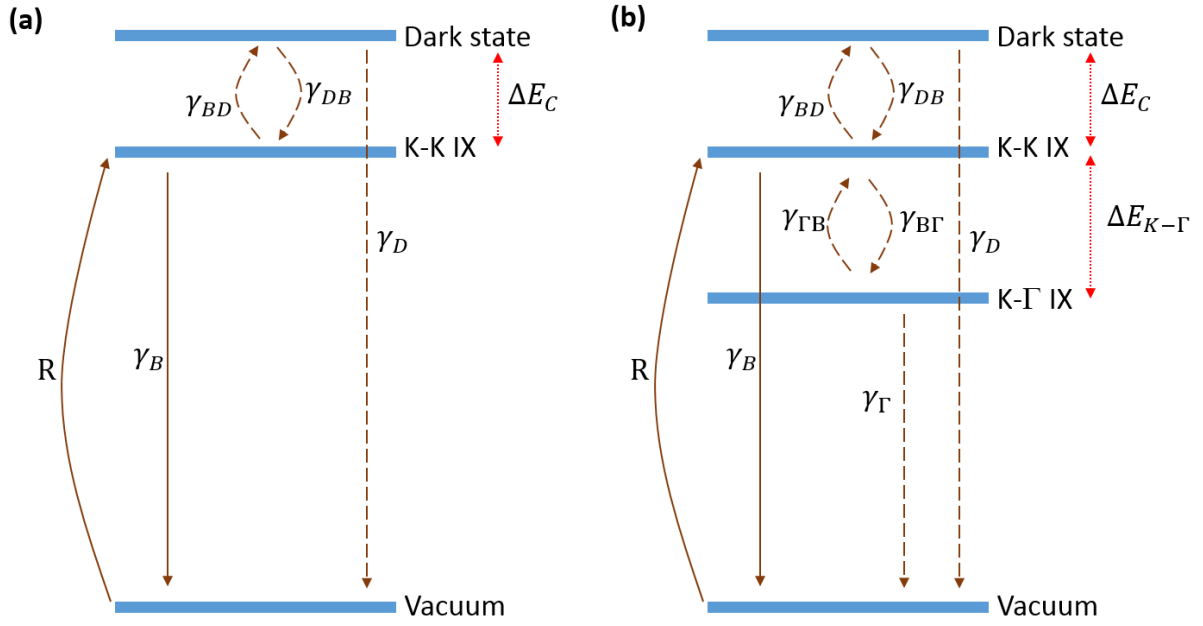


FIG. S6. (a,b) Rate equation model for Case 1 and Case 2, respectively. The solid brown lines are the optically active transition. The dashed brown lines show dark transitions (either non-radiative or optical emission cannot be collected). The total population is conserved.  $\gamma_{DB}, \gamma_{B\Gamma} \gg$  other rates.

The following relations are used:  $\gamma_{BD} = \gamma_{DB} \exp\left(-\frac{\Delta E_C}{k_B T}\right)$ ,  $\gamma_{\Gamma B} = \gamma_{B\Gamma} \exp\left(-\frac{\Delta E_{K-\Gamma}}{k_B T}\right)$  The derived

fitting parameters used in equation (S1) and (S2) are:  $A = \frac{R + \gamma_D}{R + \gamma_B}$ ,  $P = \frac{R + \gamma_B}{\gamma_{B\Gamma}}$ , and  $Q = \frac{R + \gamma_B}{\gamma_{\Gamma}}$ .

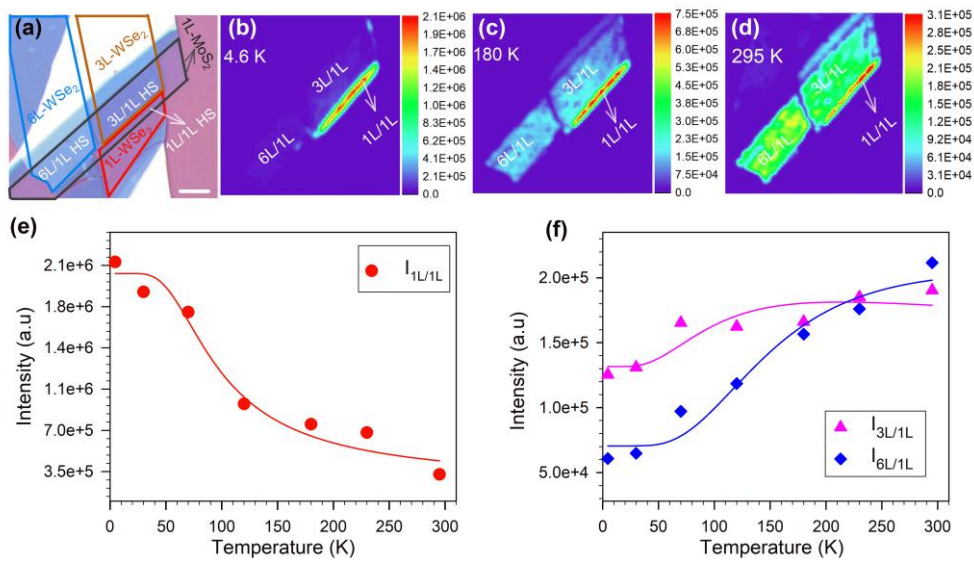


FIG. S7. (a) The optical microscope image of mL/1L ( $m=1, 3,$  and  $6$ ) HS (S3), the scale bar is  $10 \mu\text{m}$ . (b-d) PL intensity map of IXs at  $4.6 \text{ K}$ ,  $180 \text{ K}$ , and  $295 \text{ K}$ , respectively. (e-f) The PL intensities of mL/1L HS as

a function of temperature. The solid lines are the fitting results. The  $\Delta E_{K-\Gamma}$  is  $15 \pm 5$  meV in 3L WSe<sub>2</sub> and  $27 \pm 6$  meV in 6L WSe<sub>2</sub>.

#### Section IV: Additional time-resolved PL measurement data

Figure S8 shows time-resolved PL measurement data of sample S1. It shows similar trends with those observed in sample S3 (Fig. 4 in the main text), i.e.:

1. The lifetime getting shorter as the number of WSe<sub>2</sub> layers is increased,
2. As the temperature is increased, the IXs emission in 1L/1L and 2L/1L decays faster while it decays slower in the case of ( $m > 3$ )L/1L HS. In particular, the lifetime of the IXs emission in ( $m > 3$ )L/1L HS approaches that in 1L/1L HS as the temperature is increased.

Figure S9 shows the PL spectra of 1L/1L HS and 2L/1L HS in sample S2. Here the band shift is determined to be around 19 meV, which is very close to the energy difference in sample 1. This shows the repeatability of our results.

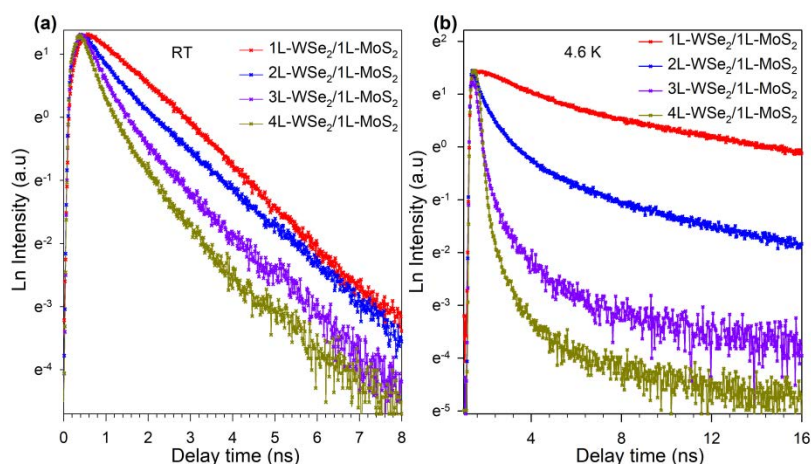


FIG. S8. (a-b) The time-resolved PL spectra of  $m$ L/1L ( $m=1, 3$  and  $6$ ) HS (S1) at room temperature and 4.6 K, respectively.

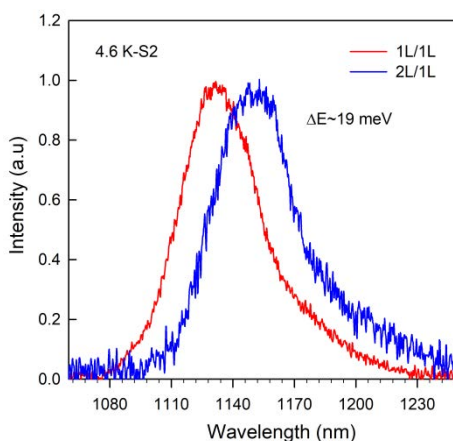


FIG. S9. Comparison between the PL spectra of 1L/1L HS vs. 2L/1L HS, showing the energy difference of the IXs emission in HS (S2) samples.

- [2] X. Luo, Y. Zhao, J. Zhang, M. Toh, C. Kloc, Q. Xiong, and S. Y. Quek, *Phys. Rev. B* **88**, 195313 (2013).
- [3] L. Liang, J. Zhang, B. G. Sumpter, Q.-H. Tan, P.-H. Tan, and V. Meunier, *ACS Nano* **11**, 11777 (2017).
- [4] X. Zhang, W. P. Han, J. B. Wu, S. Milana, Y. Lu, Q. Q. Li, A. C. Ferrari, and P. H. Tan, *Phys. Rev. B* **87**, 115413 (2013).
- [5] J.-B. Wu, H. Wang, X.-L. Li, H. Peng, and P.-H. Tan, *Carbon* **110**, 225 (2016).
- [6] P. V. Nguyen *et al.*, *Nature* **572**, 220 (2019).